

A LINEAR WEIGHTED LAPLACIAN SMOOTHING FRAMEWORK FOR WARPING TETRAHEDRAL MESHES^{*§}

SUZANNE M. SHONTZ[†] AND STEPHEN A. VAVASIS[‡]

Abstract. We present a new mesh warping framework for tetrahedral meshes based upon weighted laplacian smoothing. We start with a 3D domain that is bounded by a triangulated surface mesh and has a tetrahedral volume mesh as its interior. We then suppose that a movement of the surface mesh is prescribed and use an algorithm within our framework to update the nodes of the volume mesh. The first step is to determine a set of local weights for each interior node that describes each interior node in terms of the positions of its neighbors. After a boundary transformation is applied, a linear system of equations based upon the weights is solved to determine the final positions of the interior nodes. The three steps comprise the linear weighted laplacian smoothing (LWLS) framework. We present two methods within this framework. The first, LBWARP, uses a log-barrier approach to compute the weights. The second, FEMWARP, is based upon the finite element method. We study mesh invertibility and prove a theorem giving sufficient conditions for a mesh to resist inversion by a transformation. We prove a theorem for general mappings within the context of FEMWARP. We show that for LWLS algorithms, the resulting mesh is the same as the converged mesh obtained from the local version of weighted laplacian smoothing and from the Gauss-Seidel algorithm, when the latter two algorithms converge. We test the robustness of our algorithms and present some numerical results. Finally, we use FEMWARP to study the movement of the canine heart.

Key words. moving meshes, adaptation, optimization-based mesh smoothing, log-barrier method, finite element method, tetrahedral meshes, unstructured mesh generation, cardiology

AMS subject classifications. 65N50, 65N30, 92C10

1. Introduction. Moving meshes arise in cardiology, computer graphics, animation, and crash simulation, among other applications in science and engineering. With moving meshes, the mesh is updated at each step in time due to a moving domain boundary, thus resulting in potentially drastically varying mesh quality from step to step. One problem that can occur at each timestep is element inversion. We focus on maintaining good-quality tetrahedral meshes throughout the mesh warping process in this paper.

It is well-known that poor quality elements affect the stability, convergence, and accuracy of finite element and other solvers because they result in poorly conditioned stiffness matrices and poor solution approximation [34]. If well-shaped elements are not the result of updating the mesh boundary, the mesh quality must be improved by topological or geometrical means after each time step.

Research has shown that mesh smoothing (or r-refinement) methods can be applied to improve the quality of a mesh. These methods adjust the positions of the vertices in the mesh while preserving its topology.

Laplacian smoothing is the most popular method for node-based mesh smoothing. In an iterative manner, it repositions the vertices of the mesh by moving each interior node to the geometric center of its neighbors. It is often used because it is computationally inexpensive and is very easy to implement. However, the method has several undesirable properties. One of them is that the method is not guaranteed to work, i.e., sometimes it inverts mesh elements. A second drawback is that if the algorithm is not run to convergence, the resulting mesh depends upon the order in which the nodes are smoothed.

A related type of smoothing, namely Winslow smoothing, is more resistant to mesh folding due to the requirement that the logical variables be harmonic functions. This method was introduced for structured meshes by Winslow in [41]. In [22], Knupp extends this idea to unstructured quadrilateral meshes; he used a finite-difference method for his derivative computations. Others have used the

^{*}The work of the first author is supported by the National Physical Science Consortium, Sandia National Laboratories, and Cornell University. The work of both authors is supported in part by NSF grant ACI-0085969.

[§]A preliminary version of these results appeared in shortened form in the Proceedings of the 2003 International Meshing Roundtable.

finite element method for the derivative computations on unstructured meshes; for example, Knupp cites a proprietary DOE paper by Tipton to which the authors do not have access. (See the references at the end of [22].)

Many others have created extensions to Winslow’s method. One type of extension has been to generate the meshes using a variational approach; for example, see Brackbill and Saltzman [4], Russell and co-workers [7] and [19], and Thompson et. al [37]. Dvinsky [9] uses the theory of harmonic functions to generate a harmonic map between the physical domain and the logical domain in order to generate the mesh. Meshes that have been generated according to this method possess regularity and smoothness properties. Li et. al [24] also introduced a moving mesh method based on harmonic maps; their method has two parts: a solution algorithm and a mesh-redistribution algorithm. In doing so, they are able to obtain the desirable properties of both the h-method and r-method for finite elements.

Other, more accurate methods for r-refinement are possible. Most of these methods are based upon optimization. Optimization-based methods are used with the goal of guaranteeing an improvement in the mesh quality by minimizing a particular mesh quality metric. Their main drawback, however, is their computational expense. Examples of optimization-based methods for r-refinement can be found in the following papers: [13], [12], [11], [14], [10], [15], [1], [2], [31], [6], [39], and [42]. For a theory of algebraic mesh quality metrics see [23].

To address the above issues, Baker [3] developed a three-step method for the metamorphosis of tetrahedral meshes. Each cycle of the method involves a combination of r-refinement, mesh coarsening, and mesh enrichment to adapt the mesh. The first step in the cycle is to move the interior nodes as far as possible using r-refinement while avoiding element inversion. The second step is to remove the poorly shaped elements in the mesh using mesh coarsening. The final step is the addition of elements to improve the mesh quality by mesh refinement. This dynamic procedure was shown to be more cost-effective than just r-refinement. One disadvantage of this technique is that it comes with no theoretical guarantees as it is difficult to analyze because each cycle is a combination of three very different techniques.

We study a different mesh warping problem where the connectivity of the mesh is not allowed to change, which is important for some applications. The problem that we address is as follows: Given a 3D domain, bounded by a triangulated surface mesh, and given an interior volume mesh composed of unstructured tetrahedra, suppose the triangulated surface mesh is displaced. Is there an algorithm to move the nodes of the volume mesh so that it continues to conform to the surface mesh and to be a good quality mesh? Seeking simplicity, preservation of the mesh’s combinatorial structure, theoretical guarantees, and low computational expense, we developed a linear weighted laplacian smoothing (LWLS) framework for mesh warping in two and three dimensions. Here we describe the 2D framework; it extends to 3D in the obvious way.

The first step within the LWLS framework is to determine a set of local weights for each interior node which describes each interior node in terms of the positions of its neighbors. To this end, let (x_i, y_i) denote the x - and y -coordinates respectively of the i th interior node in the initial mesh. In addition, let the x - and y -coordinates of its adjacent vertices be given by $\{(x_j, y_j) : j \in N_i\}$, where N_i denotes the set of neighbors of node i . We denote the set of weights by w_{ij} , where w_{ij} is the weight of node j on interior node i . Each set of local weights satisfies the following set of equations:

$$x_i = \sum_{j \in N_i} w_{ij} x_j, \quad (1.1)$$

$$y_i = \sum_{j \in N_i} w_{ij} y_j, \quad (1.2)$$

$$\sum_{j \in N_i} w_{ij} = 1. \quad (1.3)$$

Below we propose two distinct methods, LBWARP and FEMWARP, for computing the w_{ij} ’s.

We first establish some necessary notation and terminology. Let b and m represent the numbers of boundary and interior nodes, respectively. Next, define x_B and y_B to be vectors of length b that contain the initial x - and y -coordinates of the boundary nodes. Similarly, let x_I and y_I be vectors of length m that contain the initial x - and y -coordinates of the interior nodes. Then $[x_B, y_B]$ and $[x_I, y_I]$ contain the original positions of the boundary and interior nodes respectively. Next, define the weighted Laplacian matrix, L , for a weighted graph $G(V; E; w)$ as follows:

$$L(i, j) = \begin{cases} -w_{ij} & \text{if } i \neq j, \\ \sum_{k \in V} w_{ik} & \text{if } i = j, \end{cases}$$

where $w_{ij} = 0$ if $(i, j) \notin E$. The boundary nodes are assumed to be numbered last.

Denote by $A = [A_I, A_B]$ the matrix that is derived from the weighted Laplacian matrix by deleting its last b rows. Note that A_I contains all of the weights corresponding to the interior neighbors and is $m \times m$. In addition, A_B contains all of the weights corresponding to the boundary neighbors and is $m \times b$. Linear equations (1.1)–(1.2) then can be expressed

$$A_I[x_I, y_I] = -A_B[x_B, y_B]. \quad (1.4)$$

The second step is to apply a user-supplied transformation to the boundary of the mesh. We denote the new positions of the boundary nodes by $[\hat{x}_B, \hat{y}_B]$.

The final step is to solve a linear system of equations for the new positions of the interior nodes. The linear system we use is the same as in (1.4), except it has a new right-hand side vector which accounts for the new positions of the boundary nodes. Thus, we solve (1.5) for $[\hat{x}_I, \hat{y}_I]$:

$$A_I[\hat{x}_I, \hat{y}_I] = -A_B[\hat{x}_B, \hat{y}_B]. \quad (1.5)$$

There are two main advantages to methods within the LWLS framework. First, if a continuous deformation of the boundary is given, then methods within the framework are valid for computing the resulting trajectory that specifies the movement of the interior nodes. In addition, these trajectories will be continuous. This is vital for some applications where continuity of motion is required. A second big advantage is that sparse matrix algorithms may be used to solve (1.5). The sparsity structure is apparent, since, on average, an interior node has six neighbors in 2D, whereas a typical 2D mesh may have hundreds, thousands, or even millions of nodes.

Within this framework, we present two methods for mesh warping in two and three dimensions. The first method, LBWARP, is based on a log-barrier method. For this method, each interior node is represented as a convex combination of its neighbors. Thus, the local weights are guaranteed to be positive, which means that nodal positions are being interpolated. A full description of the LBWARP method is given in Section 2.

The second method, FEMWARP, is based on the finite element method. The weights computed by this method can be rescaled so that they also sum to 1. The FEMWARP method often computes negative weights, especially in 3D. This corresponds to the extrapolation of nodal positions. As a general principle, interpolation is preferred over extrapolation in numerical analysis, although it is not certain whether or not this is important within this context. The FEMWARP method is described fully in Section 3.

Each of the methods has its advantages and disadvantages. The main advantage of the LBWARP method is that it always interpolates the values of the nodal positions, which is not always the case with FEMWARP. On the other hand, it is more straightforward to compute the weights for the FEMWARP method, as the LBWARP method requires that an optimization problem be solved to determine each set of local weights. In addition, because the matrix A_I is symmetric positive definite (rather than an M-matrix), the computation of the new positions for the interior nodes also proceeds at a faster rate for FEMWARP. Another big advantage of FEMWARP is that it is somewhat easier to develop the theory of this method.

In Section 4, we prove a theorem that gives sufficient conditions for when a mesh is able to resist inversion by a transformation. We also study mesh inversion within the context of the LWLS framework. In particular, we prove that all algorithms within the LWLS framework yield exact results for affine boundary transformations. In addition, we prove a theorem for more general mappings within the context of FEMWARP. We also prove a lower bound for the LBWARP weights. In Section 5, we prove that for LBWARP, the resulting mesh is the same as the converged mesh obtained from the local version of weighted laplacian smoothing and from the Gauss-Seidel algorithm. This result also holds for FEMWARP and for any LWLS method when the latter two methods converge. In Section 6, we test our algorithms on several types of mesh deformations. In Section 7, we apply FEMWARP to study the motion of the beating canine heart under normal conditions. In Section 8, we summarize our work and identify directions for future research.

2. Log-Barrier Mesh Warping (LBWARP). Our first mesh warping algorithm within the new framework is based upon a log-barrier method. The first step in the algorithm is to generate a set of local weights for each interior node that represent the relative distances of the node to each of its neighbors. We use an interior point method from nonlinear programming in order to generate these weights. The rest of the algorithm follows the LWLS framework described in Section 1: We apply a transformation to the boundary nodes. Using these new positions for the boundary nodes and the sets of weights from the original mesh, we solve a system of linear equations to determine new positions for the interior nodes. We now give a more detailed description of the weight computation.

Here we describe a nonlinear programming method for computing the weights for 2D meshes. Note that our method can be extended to 3D in the straightforward manner; however, we have not done extensive testing of our 3D implementation. In addition, this paper analyzes primarily the 2D version.

In order to find the set of weights w_{ij} , where w_{ij} is the weight of node j on interior node i , we use the log-barrier function from nonlinear programming to formulate the following optimization problem for each i :

$$\max_{w_{ij}, j \in N_i} \sum_{j \in N_i} \log(w_{ij}) \quad (2.1)$$

$$\text{subject to } w_{ij} > 0, \quad (2.2)$$

$$\sum_{j \in N_i} w_{ij} = 1, \quad (2.3)$$

$$x_i = \sum_{j \in N_i} w_{ij} x_j, \quad (2.4)$$

$$y_i = \sum_{j \in N_i} w_{ij} y_j. \quad (2.5)$$

We note that the objective function together with the constraints form a strictly convex optimization problem for which there is a unique optimum. The optimum can thus be found by an interior point method. The use of convex optimization in mesh smoothing is not a new idea. Amenta et. al developed a framework for formulating mesh smoothing problems as quasi-convex programs so that they can be optimized as generalized linear programming problems [1]. In addition, Freitag et. al developed methods for local mesh smoothing and untangling using mesh quality metrics with convex function levels sets in [10] and [15].

By starting with an initial feasible point in the interior of the space of all possible weights, we are able to solve (2.1)-(2.5) using the projected Newton method. This method can be applied to solve optimization problems of the following form:

$$\begin{aligned} & \min_x f(x) \\ & \text{subject to } Ax = b. \end{aligned}$$

The optimality conditions for the above problem are:

$$\nabla f(x) - A^T \lambda = 0 \tag{2.6}$$

$$b - Ax = 0. \tag{2.7}$$

Here λ denotes the vector of Lagrange multipliers. Note that this is a system of nonlinear equations in x and λ ; thus Newton's method can be used to solve for x and λ . However, if the initial point is feasible (i.e., $b - Ax_0 = 0$) then p_k must satisfy $Ap_k = 0$ where $x_{k+1} = x_k + p_k$, i.e., p_k is the Newton direction at iteration k . This implies that $p_k = Zv_k$ for an $(n - m)$ -dimensional vector v_k , where Z is a basis for the null space of A . It is easy to see that the resulting equation for p_k is given by

$$p_k = - (H^{-1} - H^{-1}A^T[AH^{-1}A^T]^{-1}AH^{-1}) \nabla f(x_k), \tag{2.8}$$

where $H = \nabla^2 f(x_k)$ [28].

In order to compute an initial feasible point in the interior of the solution space, we choose three of the interior node's adjacent vertices and write (x, y) as a convex combination of the positions of the three nodes. This yields three positive weights; call them w_1, w_2 , and w_3 . In order to find a set of m positive weights, the rest of the w_{ij} are initialized to ϵ , a small positive constant. Then once ϵ has been specified, linear equations (2.3) through (2.5) can be solved for new values of w_1, w_2 , and w_3 . For small values of ϵ , all of the constraint equations above will be satisfied (using the new values for the weights). An inexact linesearch is used to make ϵ as large as possible so that w_1, w_2 , and w_3 are still reasonably sized, i.e., each of them should be greater than some small tolerance.

Once the weights have been generated, as in the general LWLS framework, the input surface deformation is applied to move the boundary nodes to new locations. The final step is to use the positions of the boundary nodes and the sets of weights to simultaneously determine the final positions for the interior nodes by solving a linear system of equations. The linear equations that must be solved are given in (1.5).

We first prove that the resulting linear system has a unique solution.

THEOREM 2.1. *The linear system (1.5), which expresses the position of each interior node as a convex combination of its neighbors, has a unique solution.*

Proof. To argue that we have uniqueness when LBWARP is used to generate the weights, we classify A_I as an M -matrix which is defined as follows:

An $n \times n$ real matrix A is said to be an M -matrix if $a_{ij} \leq 0$ for all $i \neq j$ and $A^{-1} \geq 0$.

To see that A_I is an M -matrix, we make use of the following characterization theorem:

THEOREM 2.2. [40] *If $A \in \mathbf{R}^{n \times n}$ satisfies $a_{ii} > 0$, $a_{ij} \leq 0$ for all $i \neq j$, is weakly row diagonally dominant (i.e., $Ae \geq 0, \neq 0$, where e is the vector of all 1's), and is irreducible, then A is an M -matrix.*

Because the mesh is connected and a positive weight is associated with each edge, we see that A_I is irreducible. Also, A_I is diagonally dominant, as its diagonal entries are 1, and its off-diagonal entries are negative and sum to a number in $[-1, 0]$ in each row. Since there is at least one interior node adjacent to a boundary node, $A_I e_I \neq 0$, where e_I is a vector of all 1's of length m . Therefore, A_I satisfies the definition of an M -matrix by the above argument [30]. Thus, A_I is invertible, and (1.5) has a unique solution. \square

We next solve (1.5) via Gaussian elimination. Partial pivoting is not necessary, because A_I is weakly diagonally dominant. This is a major advantage, as sparse matrix algorithms are much more efficient without pivoting.

Because the nonzero pattern is symmetric, we can first apply the symmetric minimum degree ordering to the appropriate matrix in an attempt to improve the speed of the computations. The reader is referred to [17] for discussion on the computer solution of sparse linear systems. GMRES could also be used to solve the linear system instead of Gaussian elimination in an attempt to further improve the algorithm's speed although we have not tried this. See [32] for details of the GMRES algorithm and other iterative methods for solving linear systems of equations.

3. Finite Element Mesh Warping (FEMWARP). Our second mesh warping algorithm within the new framework uses the finite element method to generate the weights during the first step. These weights are different from the LBWARP weights in that they are not guaranteed to be positive. We now give a more detailed description of this algorithm.

Here we describe a piecewise-linear finite element method for computing the weights for 2D meshes. This method can also be extended to 3D in the straightforward manner. However, this paper analyzes primarily the 2D version.

Let N be the number of triangles in the mesh. In order to determine $\{w_{ij}\}$, we use a piecewise-linear finite element method to first compute the finite element discretization of the following:

$$\begin{aligned}\Delta u &= 0 \text{ on } \Omega \\ u(x, y) &= (x, y), \quad \forall (x, y) \text{ on } \partial\Omega.\end{aligned}$$

This is done by first computing the global stiffness matrix A , where $A(i, j) = \int_{\Omega} \nabla \phi_i \cdot \nabla \phi_j \, d\Omega$, where ϕ_i is a piecewise-linear shape function which satisfies $\phi_i(v_i) = 1$ and $\phi_i(v_j) = 0, \forall j \neq i$. Second, A_I and A_B are extracted from A . To this end, we set $A_I = A(1 : m, 1 : m), A_B = A(1 : m, m+1 : m+b)$. Note that symmetry in A can be used to reduce both the number of computations and amount of memory required.

Denote by $\hat{A} = [A_I, A_B], x = [x_I; x_B]$, and $y = [y_I; y_B]$. Then, $\hat{A}[x, y] = \mathbf{0}$. Furthermore, we note that for $i = 1, \dots, m$, the entries in the i th row of \hat{A} (and thus also of A) satisfy the following equations:

$$\hat{A}(i, i)x_i = \sum_{j \in N_i} -\hat{A}(i, j)x_j \tag{3.1}$$

$$\hat{A}(i, i)y_i = \sum_{j \in N_i} -\hat{A}(i, j)y_j. \tag{3.2}$$

Thus, if we set $w_{ij} = \frac{-\hat{A}(i, j)}{A(i, i)}, \forall i \neq j$, we obtain the desired set of weights.

Once the weights have been generated, the input surface deformation is applied to move the boundary nodes to new locations. The final step is to use the positions of the boundary nodes and the sets of weights to simultaneously determine the final positions for the interior nodes by solving the linear system of equations given in (1.5).

We note that this method was proposed by Baker in [3]. However, he rejected the method and chose not to develop it since he thought that a method based upon linear elasticity would be more successful, as the displacements for the x and y variables are computed in a coupled manner. We show in [36] that this is not always the case.

We first prove that the resulting linear system has a unique solution.

THEOREM 3.1. *The linear system (1.5), which expresses the position of each interior node as a linear combination of its neighbors, has a unique solution.*

Proof. It follows from [20] that A is a symmetric, positive-definite matrix. Thus, A_I is symmetric, positive-definite (and hence invertible) since it is the $m \times m$ principal submatrix of A . Note that A_B plays the role of Dirichlet boundary conditions. \square

Because the above system is positive-definite, it is next solved via a Cholesky decomposition and two triangular solves. Because a Cholesky decomposition is being used, symmetry is being taken advantage of, and pivoting is not necessary.

Consider the following application of the FEMWARP Method. Figure 3.1 shows the three steps of the mesh warping process. Note that the original mesh is shown in the top graph. A rather large deformation is then applied to the boundary, and the result is shown in the middle graph. Finally, the interior nodes are moved to new positions as is shown in the bottom graph. The final mesh is a valid mesh, that is, it has no inverted elements. This figure shows that the method demonstrates

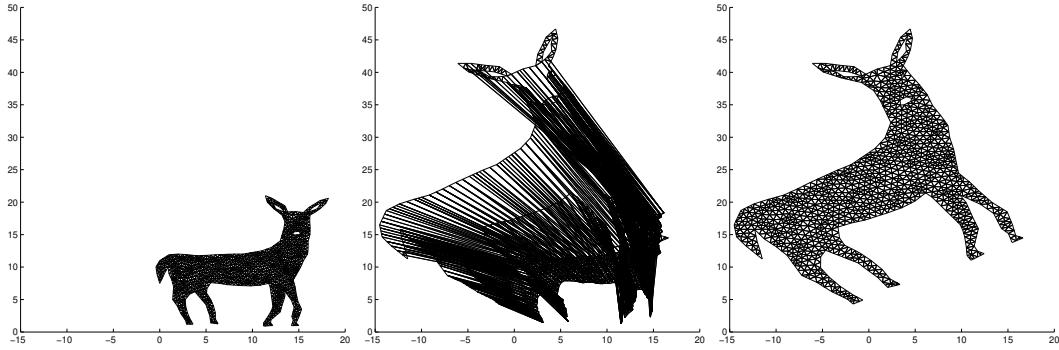


FIG. 3.1. *The three stages of the FEMWARP algorithm [16].*

promise for use as a mesh untangler in the context of the mesh warping problem.

However, the method will not always be successful. If the boundary itself becomes tangled (self-intersecting) under the deformation, then there is no possibility that FEMWARP could recover an untangled mesh. But even if the boundary is not tangled, FEMWARP may still fail as indicated by our computational experiment in Figure 3.2. Note that the shaded elements in the right box of Figure 3.2 have been inverted. In this case, the transformation applied to the boundary is too large, and it became impossible for FEMWARP to recover an untangled mesh. The same behavior is seen in LBWARP.

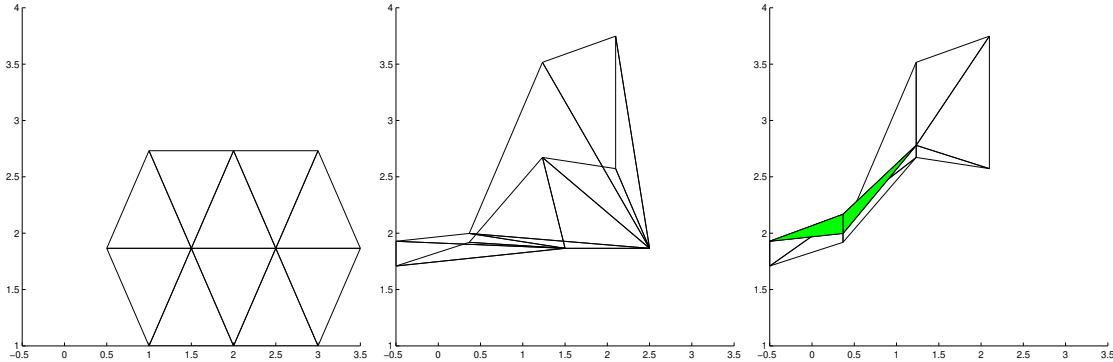


FIG. 3.2. *Two patch mesh undergoing large deformation*

Because FEMWARP and LBWARP are not guaranteed to work for all types of boundary transformations, we seek to determine what conditions will guarantee that the methods will be successful. Here we develop the theory of FEMWARP since it is easier to analyze. In order to meet this goal, we first prove a theorem about mesh invertibility and then prove a theorem on sufficient conditions for FEMWARP to be successful on the mesh warping problem.

4. Theory of Mesh Invertibility. In this section we consider sufficient conditions to guarantee that elements are not inverted in the mapped mesh. The material in this section focuses on the 2D case, but we also indicate results that extend to 3D. First, we prove a theorem about mesh invertibility in the case when a known transformation $f : \mathbf{R}^2 \rightarrow \mathbf{R}^2$ is applied to all the nodes. Then we prove a similar theorem for the case when f is applied only to the boundary and the FEMWARP algorithm is used to position interior nodes (i.e., the situation under consideration).

In order to prove Theorem 4.2 below, we first prove the following useful lemma, which has appeared in other forms in the previous literature (e.g., [26]). This lemma extends to 3D as well if “angle” in 3D means solid angle.

LEMMA 4.1. *Let K be a triangle with vertices $v_1, v_2, v_3 \in \mathbf{R}^2$. Let $A(K) = [v_2 - v_1; v_3 - v_1]$, and define the aspect ratio of K , $a(K)$, by $\frac{1}{a}$, where a is the minimum angle given in radians. Then $\frac{1}{4}a(K) \leq \kappa(A(K)) \leq 64a(K)$, where $\kappa(A(K))$ denotes the condition number of $A(K)$.*

Remark 1: There are several different ways to define aspect ratio. Knupp considers a framework for comparing the definitions in [23].

Sketch of Proof: First, we assume that the smallest angle of K is at v_1 and that $\overline{v_2v_1}$ is longer than $\overline{v_3v_1}$. The second step in the proof is to compute $\|A(K)\|$ and $\|A(K)^{-1}\|$ and show that the quantities are related to the area and edge lengths of K . Throughout the proof we use $\|\cdot\|_\infty$ for our choice of norm. The result is that $\|A(K)^{-1}\| \leq \frac{\sqrt{2}}{\text{area}(K)} l_{\max}$, where l_{\max} is the length of the longer of the edges $\overline{v_1v_2}$ and $\overline{v_2v_3}$. Similarly, it can be shown that $\|A(K)\| \leq 2\sqrt{2}l_{\max}$. Putting this together, we obtain that $\kappa(A(K))$ is bounded above by $2\frac{l_{\max}^2}{\text{area}(K)}$. Similarly, it can be shown that $\kappa(A(K))$ can be bounded below by $\frac{1}{2\text{area}(K)}l_{\min}l_{\max}$. Recall the product of an edge with its altitude is always twice the area of K . Using the relationships between side-lengths, we can rewrite our bounds as $\frac{l_{\min}}{h_{\min}} \leq \kappa(A(K)) \leq \frac{8l_{\min}}{h_{\min}}$. Now define θ to be the angle at v_1 . Because we assumed that the smallest angle is at v_1 , the longest edge is $\overline{v_2v_3}$. Therefore, $\frac{l_{\min}}{h_{\min}} = (\sin \theta)^{-1}$ and $a(K) = \frac{1}{\theta}$. So, we obtain $\frac{1}{\sin \theta} \leq \kappa(A(K)) \leq \frac{8}{\sin \theta}$. Note that $0 < \theta \leq \frac{\pi}{3}$ because θ is the smallest angle. Using basic calculus, we see that for $\theta \in [0, \frac{\pi}{3}]$, $\frac{1}{\theta} \leq \frac{1}{\sin \theta} \leq \frac{2}{\theta}$. Therefore, $a(K) = \frac{1}{\theta} \leq \frac{1}{\sin \theta} \leq \kappa(A(K)) \leq \frac{8}{\sin \theta} \leq \frac{16}{\theta} = 16a(K)$, for this specific case. It is easy to show that in the more general case, the constants differ by at most a factor of 4, i.e., $\frac{1}{4}a(K) \leq \kappa(A(K)) \leq 64a(K)$, which proves the lemma.

We are now ready to prove a theorem about mesh resistance to invertibility in the case that a transformation is applied to all nodes. This theorem is stated for 2D but extends to 3D.

THEOREM 4.2. *Suppose that $f : \mathbf{R}^2 \mapsto \mathbf{R}^2$ is bijective and differentiable on the entire mesh, with ∇f nonsingular. Suppose f is applied to all nodes of the mesh. Then no triangle in the mesh is flipped by f if inequalities (4.3) - (4.5) below hold.*

Proof. For simplicity, assume for the rest of this section that $\det(\nabla f) > 0$ on the whole mesh since the case $\det(\nabla f) < 0$ is handled symmetrically. We give sufficient conditions for the noninvertibility of the mesh elements. Let K be a triangle in the mesh with vertices v_1, v_2 , and v_3 .

Note that K is flipped by f if and only if

$$\frac{\begin{vmatrix} (v_2 - v_1)_x & (v_2 - v_1)_y \\ (v_3 - v_1)_x & (v_3 - v_1)_y \end{vmatrix}}{\begin{vmatrix} (f(v_2) - f(v_1))_x & (f(v_2) - f(v_1))_y \\ (f(v_3) - f(v_1))_x & (f(v_3) - f(v_1))_y \end{vmatrix}} < 0. \quad (4.1)$$

Using Taylor’s Theorem, we obtain:

$$\begin{aligned} f(v_2) &= f(v_1) + \nabla f(v_1)(v) \\ &+ \frac{1}{2}v^T \begin{pmatrix} \frac{\partial^2 f}{\partial x^2}(\epsilon, \mu) & \frac{\partial^2 f}{\partial x \partial y}(\epsilon, \mu) \\ \frac{\partial^2 f}{\partial x \partial y}(\epsilon, \mu) & \frac{\partial^2 f}{\partial y^2}(\epsilon, \mu) \end{pmatrix} v, \end{aligned}$$

for some (ϵ, μ) lying on the line connecting v_1 and v_2 . Here $v = \begin{bmatrix} (v_2 - v_1)_x \\ (v_2 - v_1)_y \end{bmatrix}$.

Substituting the above into (4.1) we obtain an inequality of the following form giving necessary and sufficient conditions for invertibility:

$$\frac{\begin{vmatrix} a_{11} & a_{12} \\ a_{21} & a_{22} \end{vmatrix}}{|\nabla f(v_1)| \begin{vmatrix} a_{11} + \gamma_1 & a_{12} + \gamma_2 \\ a_{21} + \gamma_3 & a_{22} + \gamma_4 \end{vmatrix}} < 0 \quad (4.2)$$

So, Lemma 2.7.1 in [18] applies to (4.2) once we have sufficient conditions for the hypotheses to hold. Note that the portion of the lemma we used states that if A is invertible, if $M = A + \sigma A$ satisfies $\|\sigma A\| \leq \epsilon \|A\|$, and if $\epsilon \kappa(A) < 1$, then M is nonsingular. Here $\kappa(A)$ denotes the condition number of A .

Using algebra and Lemma 4.1 above, we find that the following conditions ensure the hypotheses of the above lemma are satisfied:

$$\frac{1}{|\nabla f(v_1)|} \left| \frac{\partial^2 f_1}{\partial x^2}(\epsilon, \mu) \right| \leq \frac{2}{195} \frac{h_{\min}}{a(K)h_{\max}^2} \quad (4.3)$$

$$\frac{1}{|\nabla f(v_1)|} \left| \frac{\partial^2 f_1}{\partial x \partial y}(\epsilon, \mu) \right| \leq \frac{1}{195} \frac{h_{\min}}{a(K)h_{\max}^2} \quad (4.4)$$

$$\frac{1}{|\nabla f(v_1)|} \left| \frac{\partial^2 f_1}{\partial y^2}(\epsilon, \mu) \right| \leq \frac{2}{195} \frac{h_{\min}}{a(K)h_{\max}^2}, \quad (4.5)$$

where h_{\min} and h_{\max} are the smaller and larger altitudes (respectively) from v_2 and v_3 . Similar conditions are obtained for f_2 . \square

Note that this proof generalizes to higher dimensions and is thus applicable to unstructured mesh generation in 3D.

Next, we prove a theorem for FEMWARP, which is formally reminiscent of Theorem 4.2.

THEOREM 4.3. *Suppose that $f : \mathbf{R}^2 \mapsto \mathbf{R}^2$ is bijective and differentiable on the entire mesh, with $\nabla f(\mathbf{x})$ nonsingular. Let F be a conformal mapping from the unit disk, D , to the meshed region, R . In addition, assume that there exist positive constants α, β, γ , and δ such that $\|\nabla F(\mathbf{x})\|_2 \leq \alpha$, $\|\nabla^2 f(\mathbf{x})\|_2 \leq \beta$, $\|\nabla F(\mathbf{x})^{-1}\|_\infty \leq \gamma$, and $\|\nabla f(\mathbf{x})^{-1}\|_\infty \leq \frac{1}{2\delta}$. Consider transforming the mesh by applying f only to the boundary nodes of the triangulation, and then using FEMWARP to position the interior nodes. Then no triangles are flipped provided that $20\alpha\beta\gamma h + O(h^2) \leq \delta h_{\min}$, where h and h_{\min} are the maximum edge-length and minimum altitude, respectively, of any triangle in the quasi-uniform mesh.*

Remark 1: The condition in Theorem 4.3 is analogous to the hypotheses in Theorem 4.2, namely, a condition for invertibility that relates the first and second derivatives of f . There is a qualitative difference, however, between the two theorems. Theorem 4.2 states that as long as f is bijective, then for a sufficiently refined mesh (with bounded aspect ratio), there will be no inversions. On the other hand, Theorem 4.3 indicates that the condition for occurrence of inversions in the FEMWARP algorithm depends on f and the mesh aspect ratio but not so much on the level of refinement.

Remark 2: The assumptions on F are unrealistic in many cases; however, the theorem gives an idea of the important factors controlling inversion of mesh elements. They are element quality and bounding the size of the second derivative in terms of the size of the first derivative.

Proof. In considering how to prove the theorem, let us fix a particular triangle K in the original mesh, centered at (x_c, y_c) with vertices v_1, v_2, v_3 . As noted above, the positions of the nodes in the updated mesh are obtained from solving $A_I[\hat{x}_I, \hat{y}_I] = -A_B[\hat{x}_B, \hat{y}_B]$, for $[\hat{x}_I, \hat{y}_I]$ given that $[\hat{x}_B, \hat{y}_B]$ are obtained from the original $[x_B, y_B]$. In fact, each two-element row of $[\hat{x}_B, \hat{y}_B]$ is f applied to

the corresponding row of $[x_B, y_B]$. Let W_K be the $2 \times m$ matrix with 1's in the $(1, v_2)$ and $(2, v_3)$ positions and -1 's in the $(1, v_1)$ and $(2, v_1)$ positions. Then $W_K[\hat{x}_I, \hat{y}_I]$ is the 2×2 matrix, call it $A(\hat{K})$, whose determinant must be positive to avoid inversion. Thus,

$$A(\hat{K}) = -W_K A_I^{-1} A_B [\hat{x}_B, \hat{y}_B] = -W_K A_I^{-1} A_B \begin{bmatrix} f(x_{B1}, y_{B1}) \\ f(x_{B2}, y_{B2}) \\ \vdots \\ f(x_{Bb}, y_{Bb}) \end{bmatrix}, \quad (4.6)$$

where $(x_{B1}, y_{B1}), \dots, (x_{Bb}, y_{Bb})$ is an explicit enumeration of the nodes of $[x_B, y_B]$. Next, expand f as a Taylor series about (x_c, y_c) . The Taylor expansion has the form

$$f(x, y) = f(x_c, y_c) + \nabla f(x_c, y_c) ((x, y) - (x_c, y_c)) + \tilde{f}(x, y),$$

where $\tilde{f}(x, y) = f(x, y) - f(x_c, y_c) - \nabla f(x_c, y_c) ((x, y) - (x_c, y_c))$.

Claim. \tilde{f} depends only on $\nabla^2 f$, i.e., if f, g satisfy $\nabla^2 f = \nabla^2 g$, then $\tilde{f} = \tilde{g}$.

Proof. Let $\nabla^2 f$ be given. Define $\mathbf{x} = (x, y)$ and $\mathbf{x}_c = (x_c, y_c)$. We construct f from $\nabla^2 f$ using line integrals, i.e.,

$$\begin{aligned} f(\mathbf{x}) &= f(\mathbf{x}_c) + \int_0^1 \nabla f(t\mathbf{x} + (1-t)\mathbf{x}_c) \cdot (\mathbf{x} - \mathbf{x}_c) dt \\ &= f(\mathbf{x}_c) + \nabla f(\mathbf{x}_c) (\mathbf{x} - \mathbf{x}_c) \\ &\quad + \int_0^1 \int_0^1 \nabla^2 f(st\mathbf{x} + s(1-t)\mathbf{x}_c + (1-s)\mathbf{x}_c) \cdot (\mathbf{x} - \mathbf{x}_c) \cdot t \cdot (\mathbf{x} - \mathbf{x}_c) ds dt. \end{aligned} \quad (4.7)$$

From this formula, it is clear that $\tilde{f}(\mathbf{x})$ depends only upon $\nabla^2 f(\mathbf{x})$. \square

We substitute the Taylor expansion into (4.6) to obtain

$$\begin{aligned} A(\hat{K}) &= - \left(W_K A_I^{-1} A_B \begin{bmatrix} f(x_c, y_c) + \nabla f(x_c, y_c) ((x_{B1}, y_{B1}) - (x_c, y_c)) \\ f(x_c, y_c) + \nabla f(x_c, y_c) ((x_{B2}, y_{B2}) - (x_c, y_c)) \\ \vdots \\ f(x_c, y_c) + \nabla f(x_c, y_c) ((x_{Bb}, y_{Bb}) - (x_c, y_c)) \end{bmatrix} \right. \\ &\quad \left. + W_K A_I^{-1} A_B \begin{bmatrix} \tilde{f}(x_{B1}, y_{B1}) \\ \tilde{f}(x_{B2}, y_{B2}) \\ \vdots \\ \tilde{f}(x_{Bb}, y_{Bb}) \end{bmatrix} \right). \end{aligned} \quad (4.8)$$

Note that the first term is an affine mapping of x_B, y_B , whereas the second term is a finite-difference on the finite element solution to $\nabla^2 u = 0$, where $u(x, y) = \tilde{f}(x, y)$ for $(x, y) \in \partial R$, where u is the perturbation and R is the meshed region.

We can further simplify (4.8) by writing the first two terms of the Taylor expansion of f as $v^T + [x, y]L$, where L is a 2×2 matrix and v^T is 2-vector, i.e., in the general form for an affine mapping, where L and v^T depend on the choice of triangle K . (The dependence on K is not explicitly denoted.) Thus,

$$f(x, y) = v^T + [x, y]L + \tilde{f}(x, y).$$

We substitute this into (4.8) to obtain

$$A(\hat{K}) = -W_K A_I^{-1} A_B \left(e_B v^T + [x_B, y_B]L + \begin{bmatrix} \tilde{f}(x_{B1}, y_{B1}) \\ \vdots \\ \tilde{f}(x_{Bb}, y_{Bb}) \end{bmatrix} \right), \quad (4.9)$$

where e_B is vector of all 1's of length b . We can analyze the sum of the first two terms on the right-hand side explicitly using the following lemma.

LEMMA 4.4. *Suppose the boundary transformation applied to the initial mesh is an affine mapping. Then if any algorithm within the LWLS framework is used to reposition the interior nodes, the resulting mesh is the same as if the affine mapping were applied to all nodes in the initial mesh.*

This lemma extends to 3D as well.

Proof. Continuing to use the above notation, we note that the positions of the interior nodes in the deformed mesh are given by

$$[\hat{x}_I, \hat{y}_I] = -A_I^{-1} A_B ([x_B, y_B]L + e_B v^T). \quad (4.10)$$

In order to show that affine mappings yield exact results with any algorithm within the framework, we want to show that (4.10) is the same as:

$$[\hat{x}_I, \hat{y}_I] = [x_I, y_I]L + e_I v^T. \quad (4.11)$$

Observe that the equivalence of (4.10) and (4.11) would follow immediately from:

$$A_I([x_I, y_I]L + e_I v^T) = -A_B([x_B, y_B]L + e_B v^T). \quad (4.12)$$

Thus, it remains to check that (4.12) holds.

Because the weights for each interior node sum to 1, $Ae = \mathbf{0}$; i.e., $A_I e_I + A_B e_B = \mathbf{0}$. Hence $(A_I e_I + A_B e_B)v^T = \mathbf{0}$. Also, because $[x_I, y_I]$ and $[x_B, y_B]$ denote the original positions of the nodes, we know that $A_I[x_I, y_I] + A_B[x_B, y_B] = \mathbf{0}$ by (1.4). So, $(A_I[x_I, y_I] + A_B[x_B, y_B])L = \mathbf{0}$.

Putting these together, we see that

$$(A_I[x_I, y_I] + A_B[x_B, y_B])L + (A_I e_I + A_B e_B)v^T = \mathbf{0}. \quad (4.13)$$

Therefore, (4.12) holds, and the lemma is proven. \square

Substituting the result of this lemma into (4.9) and using the fact that $W_K e_I = \mathbf{0}$ (by definition of W_K) yields

$$A(\hat{K}) = W_K [x_I, y_I]L - W_K A_I^{-1} A_B \begin{bmatrix} \tilde{f}(x_{B1}, y_{B1}) \\ \vdots \\ \tilde{f}(x_{Bb}, y_{Bb}) \end{bmatrix}. \quad (4.14)$$

Observe that this equation is in a form analogous to the proof of Theorem 4.2: the matrix whose determinant we must take is written as the product of a determinant in the original mesh (namely $W_K[x_I, y_I]$) by the first derivative of f locally (namely, L) plus a remainder term. We now wish to argue that the linear term dominates the remainder term under suitable assumptions.

Lemma 4.4 allows us to partition any LWLS algorithm into an affine part and a perturbation. To do this, write $[\hat{x}_B, \hat{y}_B] = [\bar{x}_B, \bar{y}_B] + [\tilde{x}_B, \tilde{y}_B]$, where $[\bar{x}_B, \bar{y}_B]$ and $[\tilde{x}_B, \tilde{y}_B]$ denote the affine and perturbed parts of $[\hat{x}_B, \hat{y}_B]$. Similarly, $[\hat{x}_I, \hat{y}_I] = [\bar{x}_I, \bar{y}_I] + [\tilde{x}_I, \tilde{y}_I]$. Then

$$[\tilde{x}_B, \tilde{y}_B] = \begin{bmatrix} \tilde{f}(x_{B1}, y_{B1}) \\ \vdots \\ \tilde{f}(x_{Bb}, y_{Bb}) \end{bmatrix}, \text{ and the equation } A_I[\tilde{x}_I, \tilde{y}_I] + A_B[\tilde{x}_B, \tilde{y}_B] = \mathbf{0} \text{ is a discretization of}$$

Laplace's equation on the mesh domain, in which the boundary condition is a Dirichlet condition of $\tilde{f}(x, y)$ at the boundary nodes. The quantity under consideration is

$$-W_K A_I^{-1} A_B [\tilde{x}_B, \tilde{y}_B].$$

Let u_h be the piecewise-linear interpolant of \tilde{x}_I on the whole mesh. The analysis for \tilde{y}_I is the same. Also, let \tilde{J}_K denote the following scaled Jacobian on K :

$$\tilde{J}_K = \begin{bmatrix} \frac{(v_2 - v_1)_x}{\chi} & \frac{(v_2 - v_1)_y}{\chi} \\ \frac{(v_3 - v_1)_x}{\chi} & \frac{(v_3 - v_1)_y}{\chi} \end{bmatrix},$$

where χ is the maximum edge-length in K . Define m to be the m -vector of the evaluation of the finite element solution at the nodal points. Then $m(i) = u_h(v_i)$. Thus

$$\begin{aligned} -W_K A_I^{-1} A_B \tilde{x}_B &= W_K m \\ &= \begin{bmatrix} u_h(v_2) - u_h(v_1) \\ u_h(v_3) - u_h(v_1) \end{bmatrix} \\ &= \begin{bmatrix} (v_2 - v_1) \cdot \nabla u_h \\ (v_3 - v_1) \cdot \nabla u_h \end{bmatrix} \\ &= \begin{bmatrix} (v_2 - v_1)_x & (v_2 - v_1)_y \\ (v_3 - v_1)_x & (v_3 - v_1)_y \end{bmatrix} \begin{bmatrix} \frac{\partial u_h^1}{\partial x} \\ \frac{\partial u_h^2}{\partial x} \end{bmatrix} \\ &= \chi \begin{bmatrix} \frac{(v_2 - v_1)_x}{\chi} & \frac{(v_2 - v_1)_y}{\chi} \\ \frac{(v_3 - v_1)_x}{\chi} & \frac{(v_3 - v_1)_y}{\chi} \end{bmatrix} \begin{bmatrix} \frac{\partial u_h^1}{\partial x} \\ \frac{\partial u_h^2}{\partial x} \end{bmatrix} \\ &= \chi \tilde{J}_K \nabla u_h|_K. \end{aligned} \tag{4.15}$$

This demonstrates that each entry of $-W_K A_I^{-1} A_B [\tilde{x}_B, \tilde{y}_B]$ (by definition of W_K) is a finite difference of two entries of \tilde{f} at neighboring mesh nodes of triangle K centered at x_c, y_c .

Our goal is to determine a bound for $\|\nabla u_h|_K\|_\infty$. To this end, we write $\|\nabla u_h|_K\|_\infty = \|\nabla u|_K\|_\infty + \|(\nabla u_h - \nabla u)|_K\|_\infty$, where u is the solution to Laplace's equation on R with Dirichlet boundary condition $u(x, y) = \tilde{f}_1(x, y)$ on ∂R . Here \tilde{f}_1 denotes the first component of \tilde{f} . Similar notation will be used to denote the first component of various functions. Define $\hat{f} = \tilde{f}_1 \circ F$, where F is a conformal mapping from the unit disk, D , to the meshed region, R . Take $F(r, \theta) = (x_c, y_c)$. In order to determine an upper bound for $\|\nabla u_h|_K\|_\infty$, we determine \hat{u} , harmonic, such that $\hat{u} = \hat{f}$ on ∂D . Then we compute an upper bound for $\|\nabla \hat{u}\|_\infty$ from a Poisson integral analysis. Finally, we relate $\|\nabla \hat{u}\|_\infty$ to $\|\nabla u|_K\|_\infty$ via the formula $\nabla u(F(r, \theta)) = \nabla \hat{u}(r, \theta)(\nabla F(r, \theta))^{-1}$.

The Poisson integral we are interested in is

$$\hat{u}(r, \theta) = \frac{1}{2\pi} \int_0^{2\pi} \frac{(1 - r^2)\hat{u}(1, \phi)}{1 - 2r \cos(\phi - \theta) + r^2} d\phi. \tag{4.16}$$

Differentiating (4.16) with respect to r and θ yields

$$\begin{aligned}\frac{\partial \hat{u}}{\partial r} &= \frac{1}{2\pi} \int_0^{2\pi} \frac{(-2r)\hat{u}(1, \phi)(1 - 2r \cos(\phi - \theta) + r^2) - (1 - r^2)\hat{u}(1, \phi)(-2 \cos(\phi - \theta) + 2r)}{(1 - 2r \cos(\phi - \theta) + r^2)^2} d\phi, \\ \frac{\partial \hat{u}}{\partial \theta} &= \frac{1}{2\pi} \int_0^{2\pi} \frac{(1 - r^2)\hat{u}(1, \phi)(-2r \sin(\phi - \theta))}{(1 - 2r \cos(\phi - \theta) + r^2)^2} d\phi.\end{aligned}$$

Let d be the distance from $(1, \phi)$ to (r, θ) in polar coordinates. Then $d = (1 + r^2 - 2r \cos(\phi - \theta))^{\frac{1}{2}}$, and

$$\begin{aligned}\frac{\partial \hat{u}}{\partial r} &= \frac{1}{2\pi} \int_0^{2\pi} \frac{(-2r)\hat{u}(1, \phi)(1 - 2r \cos(\phi - \theta) + r^2) - (1 - r^2)\hat{u}(1, \phi)(-2 \cos(\phi - \theta) + 2r)}{d^4} d\phi, \\ \frac{1}{r} \frac{\partial \hat{u}}{\partial \theta} &= \frac{1}{2\pi} \int_0^{2\pi} \frac{(1 - r^2)\hat{u}(1, \phi)(-2 \sin(\phi - \theta))}{d^4} d\phi.\end{aligned}$$

Note that $\nabla \hat{u} = \left(\frac{\partial \hat{u}}{\partial r}, \frac{1}{r} \frac{\partial \hat{u}}{\partial \theta} \right)$ in rotated coordinates.

We are interested in the case when $\hat{u}(1, \phi) = \tilde{g}(1, \phi) = (\tilde{f}_1 \circ F)(1, \phi)$. To this end, set $\hat{u}(1, \phi) = \tilde{g}(1, \phi) = \tilde{f}_1(F(1, \phi))$.

Substituting $\tilde{g}(1, \phi)$ into the appropriate integrals, we obtain

$$\begin{aligned}\frac{\partial \hat{u}}{\partial r} &= \frac{1}{2\pi} \int_0^{2\pi} \frac{\tilde{g}(1, \phi)((-2r)(1 - 2r \cos(\phi - \theta) + r^2) - (1 - r^2)(-2 \cos(\phi - \theta) + 2r))}{d^4} d\phi \quad (4.17) \\ \frac{1}{r} \frac{\partial \hat{u}}{\partial \theta} &= \frac{1}{2\pi} \int_0^{2\pi} \frac{\tilde{g}(1, \phi)(1 - r^2)(-2 \sin(\phi - \theta))}{d^4} d\phi. \quad (4.18)\end{aligned}$$

Our goal is to get estimates on the size of these integrals. To this end, we obtain bounds on each term in their integrands as follows. First, we see that

$$\begin{aligned}|\tilde{g}(1, \phi)| &= |\tilde{f}_1(F(1, \phi))| \\ &\leq \max \|\nabla^2 f(\mathbf{x})\|_2 \|F(1, \phi) - \mathbf{x}_c\|_2^2 \text{ by (4.7)} \\ &\leq \max \|\nabla^2 f(\mathbf{x})\|_2 \alpha \|(1, \phi) - F^{-1}(\mathbf{x}_c)\|_2^2 \\ &= \max \|\nabla^2 f(\mathbf{x})\|_2 \alpha d^2 \\ &= \alpha \beta d^2.\end{aligned}$$

Let $\tau(r, \theta)$ denote the other factor in the numerator of (4.17). Then

$$\begin{aligned}\tau(r, \theta) &= (-2r)(1 - 2r \cos(\phi - \theta) + r^2) - (1 - r^2)(-2 \cos(\phi - \theta) + 2r) \\ &= -4r + 2r^2 \cos(\phi - \theta) + 2 \cos(\phi - \theta) \\ &= -4r + (2r^2 + 2) \cos(\phi - \theta) \\ &= -4r + (2r^2 + 2) \left(1 - \sin^2 \left(\frac{\phi - \theta}{2} \right) \right).\end{aligned} \quad (4.19)$$

The last equality holds as $\cos(\phi - \theta) = \cos \left(2 \left(\frac{\phi - \theta}{2} \right) \right) = 1 - 2 \sin^2 \left(\frac{\phi - \theta}{2} \right)$. Note that (4.19) is equal to

$$2(r - 1)^2 - (2r^2 + 2) \sin^2 \left(\frac{\phi - \theta}{2} \right).$$

Define $s = 1 - r$. Then

$$\begin{aligned}2(r - 1)^2 &= 2s^2 \\ &\leq 2d^2\end{aligned}$$

and

$$(2r^2 + 2) \sin^2 \left(\frac{\phi - \theta}{2} \right) \leq 4 \sin^2 \left(\frac{\phi - \theta}{2} \right).$$

In determining an upper bound for $\sin^2 \left(\frac{\phi - \theta}{2} \right)$, there are two cases to consider.

First, we show that $|\sin(\phi - \theta)| \leq d$, as this result will be used in Case 1 below. To see this, notice that

$$0 \leq (r - \cos(\phi - \theta))^2.$$

Hence,

$$\sin^2(\phi - \theta) \leq \sin^2(\phi - \theta) + (r - \cos(\phi - \theta))^2 = d^2.$$

Therefore,

$$|\sin(\phi - \theta)| \leq d.$$

Case 1: $|\phi - \theta| \leq \frac{\pi}{2}$

It follows from the above inequality that

$$\left| 2 \sin \left(\frac{\phi - \theta}{2} \right) \cos \left(\frac{\phi - \theta}{2} \right) \right| \leq d.$$

In this case, $\left| \cos \left(\frac{\phi - \theta}{2} \right) \right| \geq \cos \left(\frac{\pi}{4} \right) = \frac{\sqrt{2}}{2}$. Thus,

$$\left| \sin \left(\frac{\phi - \theta}{2} \right) \right| \frac{\sqrt{2}}{2} \leq \left| \sin \left(\frac{\phi - \theta}{2} \right) \cos \left(\frac{\phi - \theta}{2} \right) \right| \leq \frac{d}{2}.$$

This implies that

$$\left| \sin^2 \left(\frac{\phi - \theta}{2} \right) \right| \leq \frac{1}{2} d^2.$$

Case 2: $|\phi - \theta| \geq \frac{\pi}{2}$

Then

$$\left| \sin \left(\frac{\phi - \theta}{2} \right) \right| \leq 1.$$

In addition, $d \geq 1$, as $\cos(\phi - \theta) \leq 0$ for $|\phi - \theta| \geq \frac{\pi}{2}$. So,

$$d \geq \left| \sin \left(\frac{\phi - \theta}{2} \right) \right|.$$

Hence,

$$d^2 \geq \left| \sin^2 \left(\frac{\phi - \theta}{2} \right) \right|.$$

Putting the two cases together, we see that

$$\left| \sin^2 \left(\frac{\phi - \theta}{2} \right) \right| \leq d^2.$$

Hence,

$$\left| 2(r-1)^2 - (2r^2+2)\sin^2\left(\frac{\phi-\theta}{2}\right) \right| \leq 6d^2.$$

Let $\rho(r, \theta)$ denote the second term of the numerator in (4.18). Finally, we wish to determine an upper bound for $|\rho(r, \theta)|$. Observe that

$$\begin{aligned} |\rho(r, \theta)| &= 2|\sin(\phi - \theta)| \cdot |1 - r^2| \\ &= 2|\sin(\phi - \theta)| \cdot |2s - s^2| \\ &\leq 2|\sin(\phi - \theta)| \cdot |2s| \\ &\leq 2|\sin(\phi - \theta)| \cdot 2d \\ &\leq 4d^2. \end{aligned}$$

Therefore,

$$\begin{aligned} \frac{\partial \hat{u}}{\partial r} &\leq \frac{1}{2\pi} \int_0^{2\pi} \frac{\max \|\nabla^2 f(\mathbf{x})\|_2 \alpha d^2 6d^2}{d^4} d\phi = 6\alpha\beta, \\ \frac{1}{r} \frac{\partial \hat{u}}{\partial \theta} &\leq \frac{1}{2\pi} \int_0^{2\pi} \frac{\max \|\nabla^2 f(\mathbf{x})\|_2 \alpha d^2 4d^2}{d^4} d\phi = 4\alpha\beta. \end{aligned}$$

We conclude that $\|\nabla \hat{u}(r, \theta)\|_\infty \leq 6\alpha\beta$.

For a sufficiently refined mesh containing piecewise-linear elements, we note that

$$\|u - u_h\|_{W_\infty^1(\Omega)} \leq Ch\|u\|_{W_\infty^2(\Omega)} = O(h),$$

according to Corollary 7.1.12 in [5]. Thus, it suffices to approximate $\|\nabla u_h|_K\|_\infty$ by $\|\nabla u|_K\|_\infty$.

Finally, we relate $\nabla \hat{u}(r, \theta)$, where $(r, \theta) = F^{-1}(\mathbf{x}_c)$, to $\nabla u(\mathbf{x}_c)$ via the formula $\nabla u(\mathbf{x}_c) = \nabla \hat{u}(r, \theta)(\nabla F(r, \theta))^{-1}$. This yields

$$\begin{aligned} \|\nabla u_h|_K(\mathbf{x}_c)\|_\infty &= \|\nabla u|_K(\mathbf{x}_c)\|_\infty + O(h) \\ &= \|\nabla \hat{u}(r, \theta)(\nabla F(r, \theta))^{-1}\|_\infty + O(h) \\ &\leq 6\alpha\beta\|\nabla F(r, \theta)^{-1}\|_\infty + O(h) \\ &\leq 6\alpha\beta\gamma + O(h). \end{aligned} \tag{4.20}$$

Thus, we conclude that

$$\begin{aligned} \|W_K A_I^{-1} A_B \tilde{x}_B\|_\infty &= \|\chi \tilde{J}_K \nabla u_h|_K\|_\infty \\ &\leq \chi \|\tilde{J}_K\|_\infty (6\alpha\beta\gamma + O(h)) \\ &\leq 12\alpha\beta\gamma h + O(h^2). \end{aligned} \tag{4.21}$$

Similarly,

$$\|W_K A_I^{-1} A_B[\tilde{x}_B, \tilde{y}_B]\|_\infty \leq 20\alpha\beta\gamma h + O(h^2). \tag{4.22}$$

Therefore, the overall contribution from the remainder term of (4.14) is $O(h)$. We now concern ourselves with the first term in (4.14). By an argument similar to that shown in (4.15),

$$W_K[x_I, y_I]L = \chi \tilde{J}_K \nabla f(x_c, y_c)^T.$$

Thus, this term is $O(h)$, where the constant depends upon the first derivative of f . In order to finish the proof, we note that $\det(A(\hat{K})) > 0$ whenever

$$\begin{aligned} \|W_K A_I^{-1} A_B[\tilde{x}_B, \tilde{y}_B]\|_\infty &\leq \frac{\|\chi \tilde{J}_K \nabla f(x_c, y_c)^T\|}{\kappa_\infty(\chi \tilde{J}_K \nabla f(x_c, y_c)^T)} \\ &= \frac{1}{\|(\chi \tilde{J}_K \nabla f(x_c, y_c)^T)^{-1}\|_\infty}, \end{aligned}$$

according to Lemma 2.7.1 in [18]. Thus, it remains to find an upper bound for $\|(\chi \tilde{J}_K \nabla f(x_c, y_c)^T)^{-1}\|_\infty$. It is easy to show that

$$\begin{aligned} \|(\chi \tilde{J}_K \nabla f(x_c, y_c)^T)^{-1}\|_\infty &\leq \frac{1}{\text{area}(K)} \|\nabla f(x_c, y_c)^{-T}\|_\infty \chi \\ &= \frac{2}{\epsilon} \|\nabla f(x_c, y_c)^{-1}\|_\infty \\ &\leq \frac{1}{\delta \epsilon}, \end{aligned} \tag{4.23}$$

where ϵ is the minimum altitude in triangle K , as $2 \text{ area}(K) = \chi \cdot \epsilon$.

Combining (4.21) and (4.23), we see that no triangles in the mesh are flipped provided that $20\alpha\beta\gamma h + O(h^2) \leq \delta h_{\min}$. \square

At this time, we have not proven a theorem like Theorem 4.3 for the LBWARP method. However, in this section, we prove a theorem which gives a lower bound for the LBWARP weights. In particular, we show that no weight is too close to zero as long as the mesh has bounded aspect ratio. This result will be important in contexts where positive weights are required; one such example is the setup in Section 6.

THEOREM 4.5. *There is a positive-valued function $q(a)$ such that $w_{ij} \geq q(a)$, where w_{ij} is any weight computed by the LBWARP algorithm and a is the worst (largest) aspect ratio in the mesh.*

Proof. First, for this proof we need the following claim.

Claim. Let $p = (1, 0)$ be an interior node in a bounded-aspect ratio triangulation, and suppose that all of its neighboring nodes have nonnegative x -coordinates. Let x_{\max} be the maximum x -coordinate among neighbors of p . Then $x_{\max} \leq q_0(a)$, where q_0 is a fixed function and a is the mesh aspect ratio.

The proof of claim is omitted, but we give a sketch of its main idea here. For more details, see [36]. Consider the triangle t_1 containing p and also the line segment starting at p and proceeding in the negative x direction. Since no neighbor of p has a negative x -coordinate, we conclude that this triangle t_1 has an altitude at most 1. Therefore, its maximum side-length is at most a , using the following definition of the aspect ratio: $AR = \frac{l_{\max}}{alt_{\min}}$, where l_{\max} and alt_{\min} denote the maximum side-length and minimum altitude. The triangle immediately adjacent to p , possessing one side of length at most a , therefore has maximum side-length at most a^2 , and so on. The number of triangles adjacent to p is bounded by ca , where c is a universal constant, since the minimum angle of each triangle is at least $1/(c'a)$, using the alternative definition of the aspect ratio, $AR = 1/\theta_{\min}$, where θ_{\min} is the minimum angle in the triangle. (Note that the two definitions of aspect ratio are equivalent up to a constant.) Therefore, the longest side-length among neighbors of p is a^{ca} , which is the function q_0 . A similar argument appears in [27].

Once the claim is established, we can return to the proof of the theorem, which is as follows. Fix an interior point p in the initial mesh with n neighbors, and let the optimal weights computed by the LBWARP algorithm be w_1, \dots, w_n . (Omit the second subscript since p is fixed throughout the proof.) Let the neighbors of p be $(x_1, y_1), \dots, (x_n, y_n)$, and let p itself be located at (x^p, y^p) . Since the LBWARP problem is a strictly convex optimization problem on a bounded convex set, the Lagrange multiplier conditions are necessary and sufficient for optimality [29]. These conditions are

as follows. There exist three multipliers λ, μ, ν such that

$$\begin{aligned} w_1x_1 + \cdots + w_nx_n &= x^p, \\ w_1y_1 + \cdots + w_ny_n &= y^p, \\ w_1 + \cdots + w_n &= 1, \\ \lambda x_1 + \mu y_1 + \nu &= 1/w_1, \\ &\vdots \\ \lambda x_n + \mu y_n + \nu &= 1/w_n. \end{aligned}$$

First, let us consider a very simple case that $\lambda = \mu = 0$. In this case, each w_i is equal to $1/\nu$. Since the sum of the w_i 's is 1, this means in fact that $1/\nu = 1/n$ and hence $w_i \geq 1/n$ for all i . Furthermore, $1/n > (1/(ca))$ using the argument about the number of neighbors from the proof of the claim. This shows that $w_i > q(a)$ in this special case.

The generic case is that at least one of λ, μ is nonzero. Without loss of generality, we can assume $\lambda = 1, \mu = \nu = 0$. The reason this assumption is WLOG is as follows. We can apply an arbitrary transformation of the form

$$(x, y) \mapsto (x, y) \begin{pmatrix} u & v \\ -v & u \end{pmatrix} + (k_1, k_2)$$

(with at least one of u, v nonzero) uniformly to the original data $(x_1, y_1), \dots, (x_n, y_n), (x^p, y^p)$; applying such a transformation has the effect of transforming λ, μ, ν arbitrarily as long as not both λ, μ are zero but does not change any of the aspect ratios in the original triangulation (since the above transformation is a combination of a rigid motion, a translation, and a uniform scaling).

After this transformation is applied, we can further apply a uniform translation to all the y -coordinates in the original data to force $y^p = 0$. Since $\lambda = 1$ and $\mu = \nu = 0$, we conclude from the KKT system that $x_i = 1/w_i$ so that $w_i x_i = 1$. This means that $w_1 x_1 + \cdots + w_n x_n = n$, hence $x^p = n$ so $p = (n, 0)$. Also, the relationship $x_i = 1/w_i$ means that all the x_i 's are positive. Finally, the relationship $x_i = 1/w_i$ means that $\min w_i = 1/\max x_i$. In particular, in order to have a very small w_i means that there must be a very large x_i . It follows from the claim that $\max x_i \leq nq_0(a)$, hence $\min w_i \geq 1/(nq_0(a))$. Therefore, there exists a positive-valued function $q(x)$ such that all the weights are at least $q(a)$. \square

5. Theory of the Resulting Mesh. Next, we study the resulting mesh from LBWARP and compare it with the converged meshes obtained from the local weighted Laplacian smoothing and Gauss-Seidel algorithms.

THEOREM 5.1. *The resulting mesh from the LBWARP algorithm is the same as the converged meshes from the weighted Laplacian smoothing method and the Gauss-Seidel method taken one pass at a time.*

Proof. First, we note that as proved in Theorem 2.1, unique positions result when using LBWARP to solve for positions of the interior nodes. Throughout this discussion we assume that the input transformation has already been applied to the boundary.

Now, we discuss the convergence of the Gauss-Seidel algorithm when applied to $A_I[\hat{x}_I, \hat{y}_I] = -A_B[\hat{x}_B, \hat{y}_B]$. It is well-known that this algorithm is guaranteed to converge for an M -matrix. (See [38] for the details.) Thus, according to Theorem 2.2, it will converge when applied to this system.

Next, it is easy to show the iterates produced by applying the local version of weighted Laplacian smoothing to the above linear system are the same as those obtained by applying the Gauss-Seidel algorithm. The details have been omitted.

Thus, we can compute the iterates for the local version of weighted Laplacian smoothing as follows:

$[x_I, y_I]^{(k+1)} = C[x_I, y_I]^{(k)} + F[\hat{x}_B, \hat{y}_B]$,
 where $C = (M_G^{-1}N_G)$, $F = (-M_G^{-1}A_B)$, $M_G = D + L$, $D = \text{diag}(A_I)$ and $L = \text{tril}(A_I)$, $N_G = -\text{triu}(A_I)$, and $[x_I, y_I]^{(0)} = [x_I, y_I]$.

Finally, we show that the local version of weighted Laplacian smoothing converges to the same point as LBWARP. To this end, we consider the convergence of the local version of the weighted Laplacian smoothing method. In order to study its convergence, we need to concern ourselves with

$$\lim_{k \rightarrow \infty} \left(\begin{pmatrix} C & F \\ 0 & I \end{pmatrix}^k \right). \quad (5.1)$$

Note that (5.1) is equal to

$$\begin{pmatrix} \lim_{k \rightarrow \infty} C^k & \left(\sum_{j=0}^{\infty} C^j \right) F \\ 0 & I \end{pmatrix}. \quad (5.2)$$

Now, observe that $\left(\sum_{j=0}^{\infty} C^j \right) F = (I - C)^{-1} F$. In addition, observe that A_I and $-A_B$ can be obtained from $I - C$ and F via elementary row operations since $I - C = I - M_G^{-1}N_G$ and $F = -M_G^{-1}A_B$. Thus, the desired matrices are obtained by left multiplying by M_G . This proves that $(I - C)^{-1} F = -A_I^{-1} A_B$.

The final observation to make is that the eigenvalues of C satisfy $\rho(\lambda) < 1$, which can be seen as follows. First, we note that all of the entries of C are nonnegative by definition of C . Second, we note that each row sum is less than or equal to 1 since each row is a convex combination of rows with nonnegative entries and row sums that are less than or equal to 1. In addition, there is at least one row with row sum strictly less than 1 since there is at least one interior node with a boundary neighbor. Thus, the eigenvalues of C are less than 1 in absolute value, i.e., $\lim_{k \rightarrow \infty} C^k = 0$.

Putting everything together, we see that (5.2) is equal to

$$\begin{pmatrix} 0 & -A_I^{-1} A_B \\ 0 & I \end{pmatrix}. \quad (5.3)$$

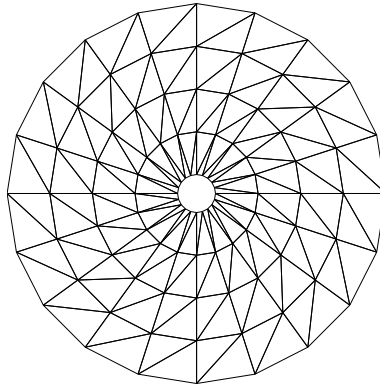
This proves the theorem, since the solution to the second linear system, $A_I[\hat{x}_I, \hat{y}_I] = -A_B[\hat{x}_B, \hat{y}_B]$, can be written as follows:

$$\begin{pmatrix} \hat{x}_I & \hat{y}_I \\ \hat{x}_B & \hat{y}_B \end{pmatrix} = \begin{pmatrix} 0 & -A_I^{-1} A_B \\ 0 & I \end{pmatrix} \begin{pmatrix} x_I & y_I \\ \hat{x}_B & \hat{y}_B \end{pmatrix}.$$

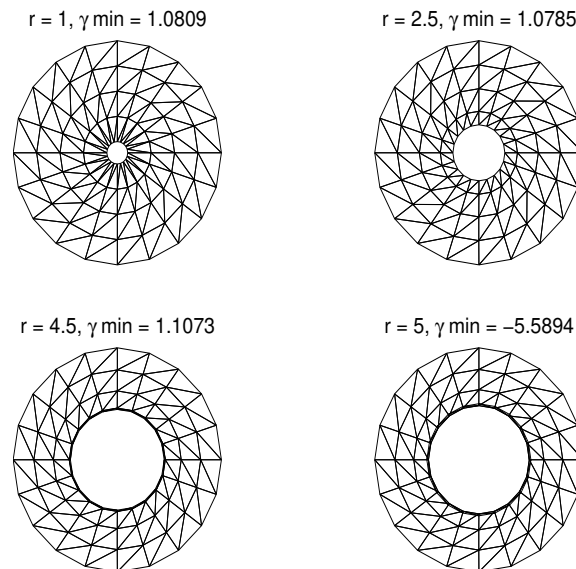
□

This result also holds for the FEMWARP algorithm, since the local weighted laplacian smoothing and Gauss-Seidel algorithms both converge for symmetric positive-definite matrices. We note that this result also holds for other algorithms within the LWLS framework whenever the local version of weighted laplacian smoothing and the Gauss-Seidel methods converge.

6. Numerical Tests. In order to test the robustness of LBWARP and FEMWARP, we designed three numerical tests each based upon a series of mesh deformations. These tests have been designed to mimic the basic elements of a beating heart's motion, namely compression and twisting. We study the heart's motion in Section 7. All of the tests involve the deformation of an annulus on each timestep. The annulus is composed of four, equally-spaced concentric rings of triangles. Its inner radius is 1, and its outer radius is 10. The initial annulus mesh is shown in Figure 6.1. For the annulus tests, we only discuss the results from the FEMWARP method, as the results obtained from LBWARP are similar.

FIG. 6.1. *Initial annulus mesh.*

In the first test, the inner circle was deformed via an outward translation on each iteration. In particular, its radius was increased by 0.5 each timestep. Figure 6.2 shows how the annulus mesh changes over time when FEMWARP was used to warp the mesh. The test showed that when the inner radius of the annulus became 5, too much deformation had occurred, since the mesh had inverted, and the minimum mean ratio of a triangle in the mesh, denoted by γ_{\min} , was less than 1. (See [13] for the mean ratio definition.) However, as this test demonstrates, FEMWARP tolerates a large amount of compression before inversion occurs.

FIG. 6.2. *Test 1: Translation of Inner Circle of Annulus by FEMWARP.*

Rotation of the inner circle occurs in the second deformation series. On each iteration, the inner circle was rotated counterclockwise 10 degrees. Figure 6.3 shows how the annulus changes over time when FEMWARP was used to warp the mesh. In each of the figures, the number of degrees the annulus has been rotated is given along with the minimum mean ratio of the triangles in the mesh. Notice that as the inner circle rotates counterclockwise, the quality of the triangles in the inner ring decreases. The mesh remained untangled until it had been rotated 70 degrees.

The goal of the third test was to combine translation and rotation of the inner circle. At each

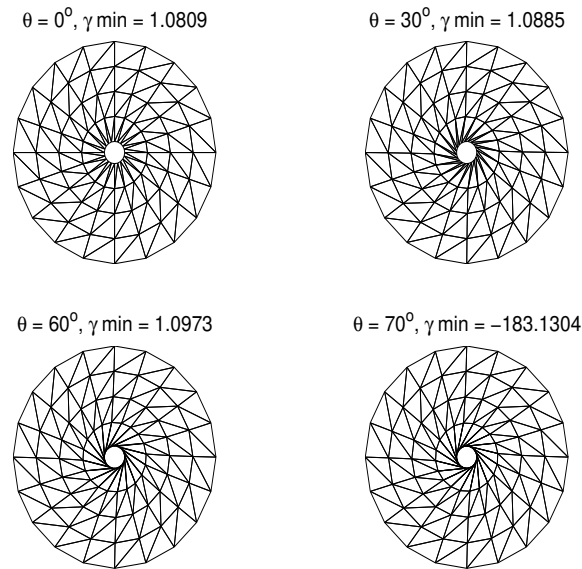


FIG. 6.3. *Test 2: Rotation of Inner Circle of Annulus by FEMWARP.*

timestep, the motions of the first two tests were combined, i.e., the radius of the inner circle was increased by 0.5, and it was rotated by 10 degrees. Figure 6.4 shows the results when FEMWARP was used for the mesh warping. The new radius for the inner circle, its amount of rotation, and the minimum mean ratio of the triangles are given. Observe that the mesh remains untangled until the radius of the inner circle is 3.5 and the circle has been rotated by 50 degrees.

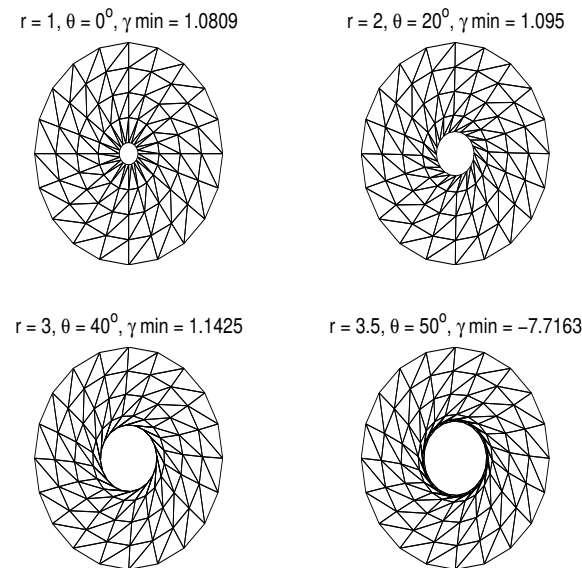


FIG. 6.4. *Test 3: Translation and Rotation of Inner Circle of Annulus by FEMWARP.*

From these three tests, we conclude that FEMWARP can withstand relatively large amounts of compression and twisting while resisting inversion. However, whenever the deformations either tangle the boundary or are too large, FEMWARP fails because inversion of elements occurs. The

same conclusions hold for the LBWARP tests.

In order to compare the LBWARP and FEMWARP methods, we chose specific nonlinear boundary deformations in order to determine how much deformation each test mesh could withstand when warped according to each method. The nonlinear deformations we used can be written as the sum of an affine mapping plus a parameter-controlled nonlinear term. In 2D, the boundary deformation used for the tests was:

$$\begin{pmatrix} x \\ y \end{pmatrix} \mapsto \begin{pmatrix} 2 & -1 \\ -2 & 5 \end{pmatrix} \begin{pmatrix} x \\ y \end{pmatrix} + \alpha \begin{pmatrix} 0.2x^2 + 0.1xy + \sin(x - \pi) \\ 0.5y^2 + 5 \sin(y) \cos(x) \end{pmatrix},$$

whereas in 3D, it was:

$$\begin{pmatrix} x \\ y \\ z \end{pmatrix} \mapsto \begin{pmatrix} 2 & -1 & 0 \\ -2 & 5 & 0 \\ 0 & 0 & 1 \end{pmatrix} \begin{pmatrix} x \\ y \\ z \end{pmatrix} + \alpha \begin{pmatrix} 0.1xy \\ 0.5yz \\ 0.1x^2 \end{pmatrix}.$$

Initially, the parameter, α , controlling the nonlinear term in each boundary deformation was set to zero. Thus, the initial warping of the mesh was done in an affine manner, which we know yields a valid mesh according to Lemma 4.4. The value of α was then increased, whereby increasing the amount of deformation to the mesh. When α became large enough, inversion eventually occurred, and its value, which we denote by α_{\max} , was recorded at that time. Table 6.1 and Table 6.2 give the results obtained from warping various 2D and 3D meshes, respectively, according to these boundary deformations.

TABLE 6.1
Values of α_{\max} for Warping Methods [16].

2D mesh	LBWARP	FEMWARP
arc	0.2	0.9
cylinder	2	2
deer	2.6	2.6
rand400	1.8	1.8
rand1000	1.8	1.8

TABLE 6.2
Values of α_{\max} for Warping Methods [21].

3D mesh	LBWARP	FEMWARP
foam	0.3	0.7
gear	1.8	3.5
hook	0.08	0.16

These results demonstrate that in 2D, LBWARP and FEMWARP often perform identically. However, it is sometimes the case that one method outperforms the other. In Table 6.1, we see that FEMWARP did better than LBWARP on the arc mesh. (We have also seen computational results that indicate that LBWARP performs better than FEMWARP at times, although those results are not included here since they were for a different boundary motion.) In 3D, the two methods often perform differently as seen in Table 6.2. For the chosen deformation, FEMWARP always outperformed LBWARP. Table 6.3 and Table 6.4 show the percentage of negative weights computed by FEMWARP for each of the test meshes. From these tables, we see that it is when the FEMWARP method computes a high percentage of negative weights that the performance of the two methods differs the most, as FEMWARP is extrapolating nodal positions under these circumstances. Counterintuitively, FEMWARP performed better than LBWARP for meshes with high percentages of negative weights.

TABLE 6.3
Percentage of Negative Weights Computed by FEMWARP[16].

2D mesh	Percent Negative Weights
arc	29.5
cylinder	0.37
deer	0.11
rand400	0
rand1000	0

TABLE 6.4
Percentage of Negative Weights Computed by FEMWARP [21].

3D mesh	Percent Negative Weights
foam	21.8
gear	24.8
hook	23.6

7. Application to Cardiology. We now use FEMWARP in order to study the movement of the beating canine heart under normal conditions. To do this, we obtained data from the Laboratory of Cardiac Energetics at the National Institutes of Health (NIH) [25]. We were given (x, y, z, t) data for 192 points on the inner surface of the left and right ventricles of the beating canine heart from a physiological pacing experiment. The data frames are 14.6 milliseconds apart with the first frame occurring 12 milliseconds before the pacing spike.

The first step in the simulation of the ventricular movement was to generate a mesh for the initial position of the ventricles. In order to do this, we first noted that the 192 points we were given were arranged in 8 slices with 24 points each. Thus, in order to generate the initial mesh, we decided to create a mesh for the top slice and then use FEMWARP to do the mesh warping necessary to create meshes for the remaining slices. Note that this uses FEMWARP in one and two dimensions as we describe in detail below. Once we have the meshes for all of the levels, we connect the triangular meshes into a tetrahedral mesh for the ventricles. The procedure to do this is also described below.

We now give a more detailed description of the method we used to create the initial mesh of the canine ventricles. We first used the two-dimensional quality mesh generation package called Triangle [33] to generate an initial mesh of the top slice (after projecting it into the x - y plane). Note that this yielded a good-quality mesh in the x - y plane with several additional nodes. Second, we computed the z -coordinates for the new points on the boundary of the top slice using 1D FEMWARP. Third, we used the weight-finding portion of our FEMWARP algorithm to compute the weights for the appropriate 2D linear system obtained from the x - and y -coordinates. Fourth, we determined the z -coordinates for the mesh of the top slice by forcing the z -coordinates to satisfy the appropriate 3D linear system using the 2D weights. At this point, we had the mesh for the top slice.

Our second task was to generate meshes for each of the remaining 7 slices. This was done using our FEMWARP algorithm to warp the mesh for the top slice into meshes for each of the remaining slices. In order to accomplish this, the first step was to determine the coordinates of the additional boundary nodes for the mesh of the appropriate slice. This was done using 1D FEMWARP. Then, the (x, y) coordinates of the interior nodes of that slice were determined using 2D FEMWARP. The z -coordinates for the interior nodes were found by forcing them to satisfy the appropriate 3D linear system using these weights.

The third step was to connect the triangular meshes for each of the 8 slices into one tetrahedral mesh for the canine ventricles. To do this, the corresponding triangles between two slices were connected to form a triangular prism. After a temporary mesh of triangular prisms was created, the

triangular prisms were subdivided into tetrahedron using the method outlined in [8].

After the initial tetrahedral mesh was created, we checked its quality using the mean ratio mesh quality metric. Using this test, it was determined that the initial mesh was of poor quality. This was because the 8 slices were equally-spaced even though the curvature of the ventricles changes much more rapidly near the bottom of the heart. Thus, we decided to use linear interpolation in conjunction with FEMWARP in the obvious way in order to add two additional slices of nodes near the bottom of the heart. Because the curvature of the ventricles changes more rapidly near the bottom of the heart, the first additional slice was placed halfway between levels 7 and 8, and the second additional slice was placed halfway between the first new level and level 8. The resulting initial mesh is shown in Figure 7.1.

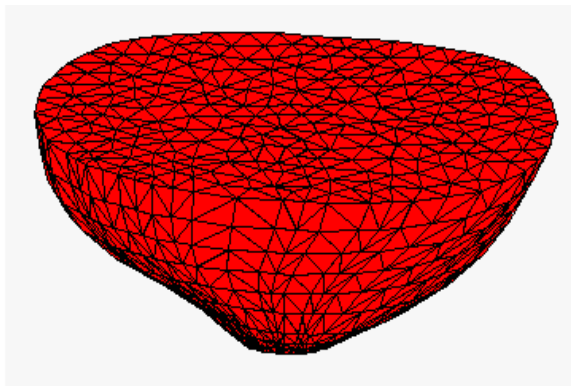


FIG. 7.1. *Initial canine ventricular mesh.*

After the initial mesh was created, the heart data was used to move the 192 data points on the boundary of the mesh to their new positions. The same process as above (i.e., FEMWARP in 1D, FEMWARP in 2D, and using 1D FEMWARP to add the two new levels of data near the bottom) was used in order to reposition the remaining boundary points. Once the boundary nodes were relocated to their positions for timestep $t = 2$, the 3D version of FEMWARP was used to move the interior nodes to their new positions for this timestep. This process was performed iteratively in order to study the movement of the heart at timesteps $t = 3, \dots, 32$.

The simulation of the canine ventricular movement produced a series of meshes that show the ventricles twisting, expanding, and then contracting over the cardiac cycle. This is consistent with what occurs in nature. These meshes were combined into an animation which can be seen at [35]. Because the dynamic range of the motion is small, it cannot be detected in single figures (separate from an animation).

During each timestep, the mean ratios of the tetrahedra in the mesh were computed. The mean ratio computations showed that the heart remained untangled throughout the entire simulation. This is not very surprising since the heart mesh is composed of elliptical rings that seem to undergo less movement on each timestep than the circular rings in the test cases. However, the motion of the heart is anisotropic which makes it difficult to predict in advance how it will tolerate deformations. Interestingly enough, the values of the minimum and average mean ratios were relatively constant across all timesteps. Only the value of the maximum mean ratio changed a significant amount. The mean ratio computations are also a good indication that the heart meshes are of sufficiently good quality for use with a numerical PDE solver that requires moving meshes.

In order to further test our mesh warping algorithm, the motion of the ventricles was exaggerated by a factor of 3. In this case, the motion was large enough to detect in separate figures and is shown in Figure 7.2. We note that the FEMWARP algorithm also performed successfully in this case, which is encouraging given the much larger deformations.

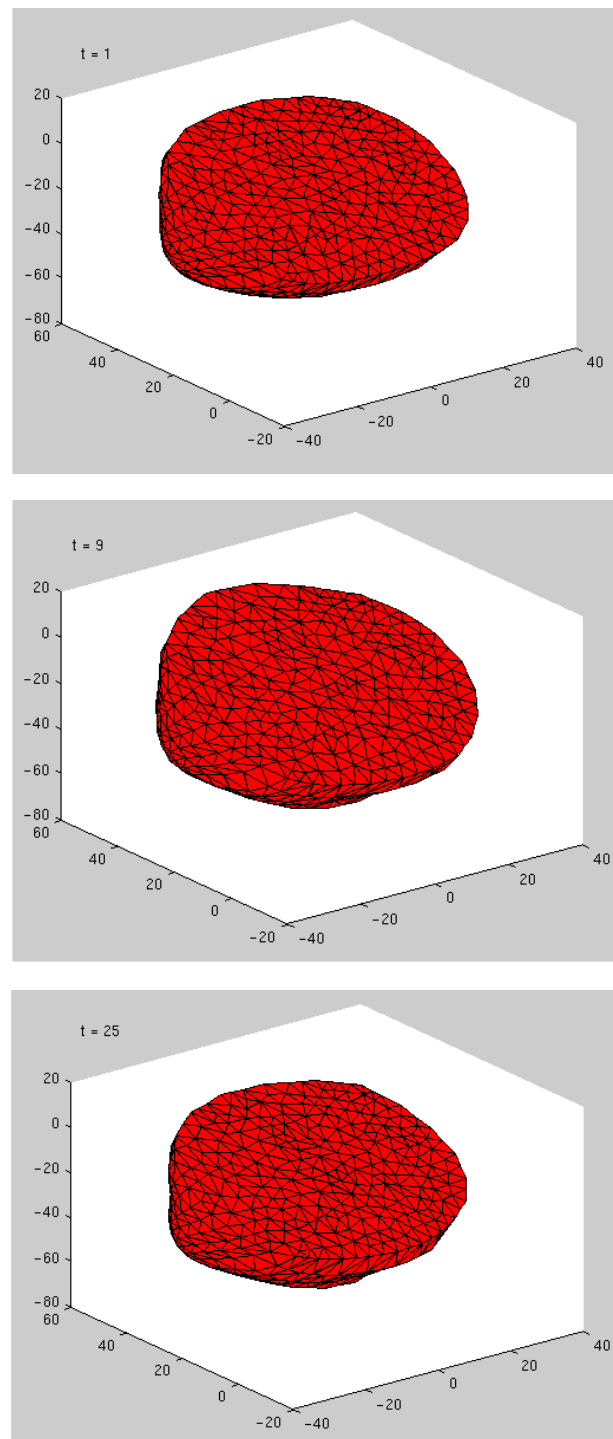


FIG. 7.2. *Exaggerated Movement of the Heart as it Beats. Motion for timesteps $t = 1, 9$, and 25 .*

8. Conclusions. In summary, we developed a linear weighted laplacian smoothing (LWLS) framework for warping tetrahedral meshes. The first step in our framework is to determine a set of local weights for each interior node. Second, a user-supplied deformation is applied to the boundary nodes. The third and final step is to solve a system of linear equations based upon the weights and the new positions of the boundary nodes to determine the final positions of the interior nodes.

Within this framework, we presented two methods: LBWARP and FEMWARP based on a log-barrier method and the finite element method, respectively. Both of these methods are simple, preserve the mesh's combinatorial structure, are computationally inexpensive, and provide some theoretical guarantees for use on the mesh warping problem.

There are two main advantages to methods within the LWLS framework. First, if a continuous boundary deformation is given, then methods within the framework are valid for computing the resulting trajectory that specifies the movement of the interior nodes. In addition, these trajectories will be continuous, which is vital for applications where continuity of motion is required. Second, sparse matrix algorithms may be used to solve the linear system which determines the final positions of the interior nodes.

We proved a theorem regarding mesh invertibility and a lemma showing that all LWLS methods yield exact results for affine boundary transformations. In addition, we proved a theorem, within the context of FEMWARP, giving sufficient conditions for the mesh to resist inversion for more general mappings.

In addition, we proved a theorem that gave a lower bound for the LBWARP weights. We also showed that the resulting mesh from any of the LWLS methods is the same as the converged mesh obtained from a local version of the algorithm and from the Gauss-Seidel method whenever the latter two methods converges.

We tested the robustness of LBWARP and FEMWARP and demonstrated computationally that FEMWARP is often more successful than LBWARP at resisting inversion of mesh elements. We also used FEMWARP to study the motion of the canine ventricles under normal conditions.

We now describe some possibilities for future research. First, we would like to develop other types of mesh warping methods that may be more successful in withstanding larger deformations. For example, various models of nonlinear elasticity could be used for this purpose. It is hoped that the nonlinearity in the equations will make the warping procedure more accurate, thus making the method more successful at resisting inversions.

Second, we would like to use our canine ventricle meshes to study the bioelectricity of the heart. To do this, we will couple the heart's electrical activity with its mechanical motion (from the FEMWARP meshes). We will then use the finite element method to simulate the electricity on the beating heart. This will yield new knowledge of the heart's activity since most of the current models have not coupled the heart's electricity with its mechanical motion.

9. Acknowledgements. The authors wish to thank O. Faris and E. McVeigh from the Laboratory of Cardiac Energetics at the National Institutes of Health for the moving canine heart data that they provided. In addition, they wish to thank Dr. Lori Freitag-Diachin of Lawrence Livermore National Laboratory and Dr. Patrick Knupp of Sandia National Laboratories for providing us with the majority of the 2D and 3D test meshes, respectively. They benefited from conversations with G. Bailey, A. Schatz, and C. Patron of Cornell; T. Tomita, formerly of Cornell; and especially H. Kesten of Cornell.

REFERENCES

- [1] N. AMENTA, M. BERN, AND D. EPPSTEIN, *Optimal point placement for mesh smoothing*, in Proceedings of 8th ACM-SIAM Symposium on Discrete Algorithms, 1997, pp. 528–537.
- [2] E. AMEZUA, M. HORMAZA, A. HERNÁNDEZ, AND M. AJURIA, *A method for the improvement of 3d solid finite-element meshes*, *Advances in Engineering Software*, 22 (1995), pp. 45–53.
- [3] T. J. BAKER, *Mesh movement and metamorphosis*, in Proceedings of the Tenth International Meshing Roundtable, Albuquerque, NM, 2001, Sandia National Laboratories, pp. 387–396.

- [4] J. U. BRACKBILL AND J. S. SALTZMAN, *Adaptive zoning for singular problems in two dimensions*, J. Computing Phys., 46 (1982), pp. 342–368.
- [5] S. C. BRENNER AND L. R. SCOTT, *The Mathematical Theory of Finite Element Methods*, Springer, 1994.
- [6] S. A. CANANN, M. B. STEPHENSON, AND T. BLACKER, *Optimsmoothing: An optimization-driven approach to mesh smoothing*, Finite Elements in Analysis and Design, 13 (1993), pp. 185–190.
- [7] W. M. CAO, W. Z. HUANG, AND R. D. RUSSELL, *A study of monitor functions for two dimensional adaptive mesh generation*, SIAM J. Sci. Comput., 20 (1999), pp. 1978–1994.
- [8] J. DOMPIERRE, P. LABBÉ, M. VALLET, AND R. CAMARERO, *How to subdivide pyramids, prisms and hexahedra into tetrahedra*, in Proceedings of the 8th International Meshing Roundtable, Albuquerque, NM, 1999, Sandia National Laboratories, pp. 195–204.
- [9] A. S. DVINSKY, *Adaptive grid generation from harmonic maps on riemannian manifolds*, J. Computing Phys., 95 (1991), pp. 450–476.
- [10] L. FREITAG, *On combining laplacian and optimization-based mesh smoothing techniques*, in AMD - Vol. 220 Trends in Unstructured Mesh Generation, ASME, 1997, pp. 37–43.
- [11] L. FREITAG AND P. KNUPP, *Tetrahedral element shape optimization via the jacobian determinant and condition number*, in Proceedings of the 8th International Meshing Roundtable, Albuquerque, NM, 1999, Sandia National Laboratories, pp. 247–258.
- [12] ———, *Tetrahedral mesh improvement via optimization of the element condition number*, Int'l. J. Numer. Meth. Engr., 53 (2002), pp. 1377–1391.
- [13] L. FREITAG, P. KNUPP, T. MUNSON, AND S. SHONTZ, *A comparison of optimization software for mesh shape-quality improvement problems*, in Proceedings of the Eleventh International Meshing Roundtable, Albuquerque, NM, 2002, Sandia National Laboratories, pp. 29–40.
- [14] L. FREITAG AND C. OLLIVIER-GOOCH, *Tetrahedral mesh improvement using swapping and smoothing*, Int'l. J. Numer. Meth. Engr., 40 (1997), pp. 3979–4002.
- [15] L. FREITAG AND P. PLASSMANN, *Local optimization-based simplicial mesh untangling and improvement*, Intl. J. Num. Methods in Engr., 49 (2000), pp. 109–125.
- [16] L. FREITAG-DIACHIN, Personal Communication.
- [17] A. GEORGE AND J. W. H. LIU, *Computer solution of large sparse positive definite systems*, Prentice-Hall, 1981.
- [18] G. H. GOLUB AND C. F. VAN LOAN, *Matrix Computations*, John Hopkins University Press, third ed., 1996.
- [19] W. Z. HUANG AND R. D. RUSSELL, *Moving mesh strategy based on a gradient flow equation for two-dimensional problems*, SIAM J. Sci. Comput., 20 (1999), pp. 998–1015.
- [20] C. JOHNSON, *Numerical solutions of partial differential equations by the finite element method*, Studentlitteratur, 1987.
- [21] P. KNUPP, Personal Communication.
- [22] ———, *Winslow smoothing on two-dimensional unstructured meshes*, Engineering with Computers, 15 (1999), pp. 263–268.
- [23] ———, *Algebraic mesh quality metrics*, SIAM Journal on Scientific Computing, 23 (2001), pp. 193–218.
- [24] R. LI, T. TANG, AND P. ZHANG, *Moving mesh methods in multiple dimensions based on harmonic maps*, J. Computing Phys., 170 (2001), pp. 562–588.
- [25] E. MCVEIGH AND O. FARIS, Personal Communication, (February 2003).
- [26] S. MITCHELL AND S. VAVASIS, *Quality mesh generation in higher dimensions*, SIAM J. Computing, 29 (2000), pp. 1334–1370.
- [27] S. A. MITCHELL, *Mesh generation with provable quality bounds*, PhD thesis, Cornell University, 1993.
- [28] S. G. NASH AND A. SOFER, *Linear and Nonlinear Programming*, McGraw-Hill, Inc., 1996.
- [29] J. NOCEDAL AND S. J. WRIGHT, *Numerical Optimization*, Springer, New York, 1999.
- [30] J. ORTEGA, *Numerical Analysis: A Second Course*, Academic Press, 1972.
- [31] V. N. PARTHASARATHY AND S. KODIYALAM, *A constrained optimization approach to finite element mesh smoothing*, Finite Elements in Analysis and Design, 9 (1991), pp. 309–320.
- [32] Y. SAAD, *Iterative methods for sparse linear systems*, Society for Industrial and Applied Mathematics, second ed., 2003.
- [33] J. SHEWCHUK, *Triangle: Engineering a 2d quality mesh generator and delaunay triangulator*, in Proceedings of the First Workshop on Applied Computational Geometry, New York, NY, 1996, Association for Computing Machinery, pp. 124–133.
- [34] ———, *What is a good linear element? interpolation, conditioning, and quality measures*, in Proceedings of the Eleventh International Meshing Roundtable, Albuquerque, NM, 2002, Sandia National Laboratories, pp. 115–126.
- [35] S. SHONTZ, www.cam.cornell.edu/~shontz/heart.html, (2003).
- [36] S. M. SHONTZ, *Efficient Numerical Methods for a Mesh Warping Problem in Cardiology*, PhD thesis, Cornell University, Expected 2004.
- [37] J. F. THOMPSON, Z. U. A. WARSI, AND C. W. MASTIN, *Numerical Grid Generation*, North-Holland, 1985.
- [38] R. VARGA, *Matrix Iterative Analysis*, Springer-Verlag, second ed., 2000.
- [39] D. WHITE AND G. RODRIGUE, *Improved vector FEM solutions of Maxwell's Equations using grid pre-conditioning*, Int'l. J. Numer. Meth. Engr., 40 (1997), pp. 3815–3837.
- [40] G. WINDISCH, *M-matrices in numerical analysis*, Teubner, 1989.

- [41] A. WINSLOW, *Numerical solution of the quasi-linear poisson equation in a nonuniform triangle mesh*, J. Comput. Phys., 1967 (1967), pp. 149–172.
- [42] P. ZAVATTIERI, E. DARI, AND G. BUSCAGLIA, *Optimization strategies in unstructured mesh generation*, Int'l. J. Numer. Meth. Engr., 39 (1996), pp. 2055–2071.